A model for ballistic transport across locally gated graphene bipolar junctions

A model for ballistic transport across locally gated graphene bipolar junctions

Nhung T T Nguyen[1], D Quang To[1] and V Lien Nguyen[2,3]

[1] Theoretical and Computational Physics Department, Institute of Physics, VAST, 10 Dao Tan,
Ba Dinh Distr., Hanoi 10000, Vietnam
[2] Institute for Bio-Medical Physics, 109A Pasteur, 1st Distr., Hochiminh city, Vietnam

E-mail: nvlien@iop.vast.ac.vn

Abstract

An alternative model of Gaussian-type potential is suggested, which allows us to describe the transport properties of the locally gated graphene bipolar junctions in all possible charge density regimes, including a smooth transition between the regimes. Using this model we systematically study the transmission probability, the resistances, the current–voltage characteristics, and the shot noise for ballistic graphene bipolar junctions of different top gate lengths under largely varying gate voltages. Obtained results on the one hand show multifarious manifestations of the Klein tunneling and the interference effects, and on the other hand describe well typical experimental data on the junction resistances.

(Some figures may appear in colour only in the online journal)

1. Introduction

Graphene, a single layer hexagonal lattice of carbon atoms [1], has emerged as a fascinating material in terms of both fundamental studies [2–4] and potential applications in electronic devices [5]. The linear energy spectrum with zero bandgap and the chirality of wavefunctions are the two most unusual characteristics of carriers in graphene that give rise to remarkable transport phenomena including backscattering suppression [6], Klein tunneling [7], anomalous quantum Hall effect [8, 9], or Veselago lensing [10]. In particular, the peculiar band structure of graphene makes possible the electrostatic control of carrier type, electron-like or hole-like, and carrier density across the neutrality point, obviating conventional semiconductor doping, for instance via ion implantation. Technologically, graphene has then an advantage in fabricating p–n junctions and then bipolar devices, using only local gates. Graphene p–n junctions not only are basic building blocks for more complex devices, but also have already been proposed in order to investigate fundamental properties of graphene itself [11, 12].

Experimentally, the locally gated graphene heterojunctions have been developed by several groups [11–18]. In general, to create a graphene bipolar junction (GBJ) one implements a design with two electrostatic gates, a global back gate and a local top gate (see figure 1(a)). A voltage V_b applied to the back gate tunes the carrier type and the carrier density in the bulk of graphene sheet, whereas a voltage V_t applied to the top gate tunes the carrier type and the carrier density in only some region below this gate. Thus, by varying independently the gate voltages, V_b and V_t, one can create graphene bipolar heterojunctions in all possible charge density regimes: p–n–p, n–p–n, p–p′–p, or n–n′–n, where, as usual, n or p refers to electrons or holes, respectively (see figure 1(b)).

Ozyilmaz *et al* studied the quantum Hall transport in graphene n–p–n junctions and observed a series of fractional quantum Hall plateaus as the local charge density varies in the p and n regions [11]. Huard *et al* measured the resistance (R) across GBJs and reported a noticeable asymmetry of the R versus V_t curves with respect to the maxima. Using a suspended 'air-bridge' top gate to avoid a decrease of the carrier mobility in the region under this gate, Gorbachev *et al* were able to fabricate ballistic graphene p–n–p junctions which show a reproducible oscillation of the junction resistance as the top gate voltage V_t varies [15]. Liu *et al* observed the Coulomb blockade in graphene nanoribbon based bipolar junctions, which indicates an emergence of the single electron transistors [17].
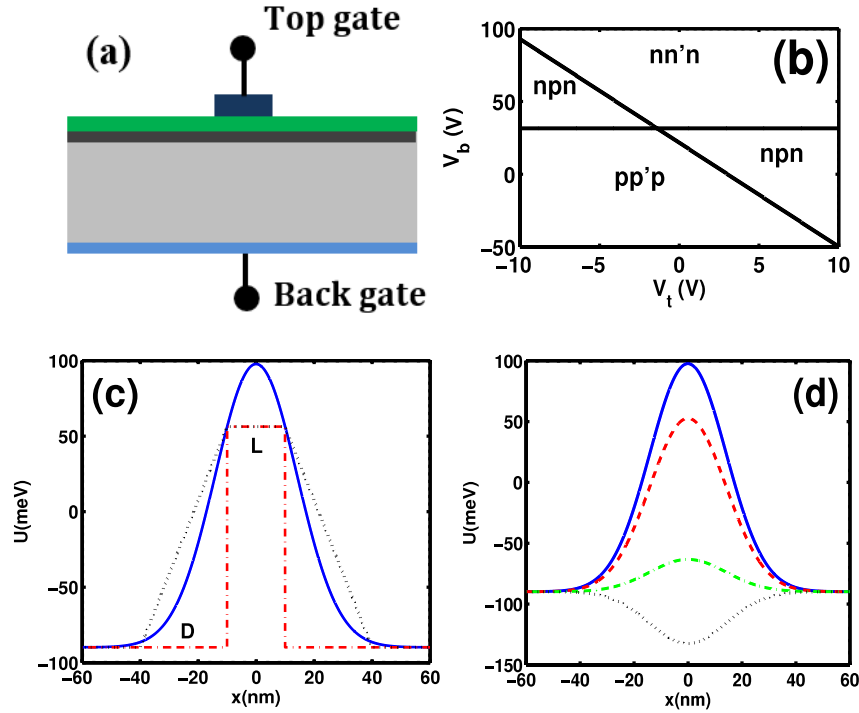
Figure 1. (a) Scheme of GBJs under study. (b) Diagram of junction charge density regimes (n for electron and p for hole). (c) Three potential barrier models in comparison: rectangular (dash–dotted line), trapezoidal (dotted line), and Gaussian (solid line). (d) Several potential profiles of equation (3): $L = 20$ nm, $V_b = 40$ V, and V_t (from top) $= -4, -3, -2$, and 0.1 V. (Other parameters are given in the text.)

Intriguing phenomena observed as well as potential applications of ballistic graphene junctions, e.g. filter circuits [7], graphene lenses [10], or single electron devices [17], have raised much interest in the ballistic regime of transport. The fact that the carrier mean free path in graphene may be as large as $l \sim 1$ μm [1, 3, 19], while the typical size of graphene based field effect transistors is only $\sim$0.25–0.5 μm [20], provides the graphene for the best material where the ballistic transport could be realized.

Theoretically, several potential models have been proposed to describe the ballistic transport across locally gated GBJs. In the simplest model of rectangular potential barriers [7, 21], the two characterizing parameters are the barrier width measuring the top gate length (L) and the barrier height turned by the two gate voltages (see figure 1(c)). Within the framework of this model the transmission probability across the junction can be exactly derived [7]:

$$\mathcal{T}(E, \theta, L) = (\cos^2\theta \, \cos^2\phi)([\cos(Lq_x) \cos\theta \cos\phi]^2 + \sin^2(Lq_x)[1 - ss' \sin\phi \sin\theta]^2)^{-1}. \quad (1)$$

Hereafter, the following symbols are addressed: E the incident energy, θ the incident angle, $k_y = k_F \sin\theta$, $\phi = \arctan(k_y/q_x)$, $q_x = \sqrt{[(E - U_2)/\hbar v_F]^2 - k_y^2}$, k_F the Fermi wavenumber, $v_F \approx 10^6$ m s^{-1} the Fermi velocity, $s = \text{sign}(E - U_1)$, $s' = \text{sign}(E - U_2)$, $U_{1(2)}(n_{1(2)}) = -\text{sign}(n_{1(2)})\hbar v_F\sqrt{\pi |n_{1(2)}|}$, n_1 the average charge density induced by the back gate voltage alone in the whole bulk of graphene sheet, and n_2 the average charge density induced by both the back gate and the top gate

voltages inside the barrier region only. For a given junction, the densities n_1 and n_2 can be defined as [8, 13]

$$n_1 = C_b(V_b - V_b^{(0)})/e \qquad \text{and}$$
$$n_2 = n_1 + C_t(V_t - V_t^{(0)})/e, \qquad (2)$$

where e the elementary charge, $C_{b(t)}$ the back (top) gate capacitance per area, and $V_{b(t)}^{(0)}$ the back (top) gate voltage required to attain the zero value of the average charge density induced by the back (top) gate. The transmission probability of equation (1) will be discussed in figures 2–4.

Another model used to describe GBJs is the trapezoidal potential barrier [13, 22, 23], taking into account the fact that the transition regions should extend for some finite range (the width D in figure 1(c)). In this model, due to the uniformity of the electric field in the transition regions, the Dirac equation has even in these regions an exact solution in terms of confluent hypergeometric functions [24], and therefore the transmission probability across the whole barrier can be in principle calculated exactly. In this way, Sonin calculated the conductance and the Fano factor for trapezoidal potential barriers of different values of D [22]. However, this study does not identify the physical nature of barrier parameters, including the source of the finite width D of transition regions, with respect to the real junctions. Low *et al* [23] tried to identify D as the typical width of the uniform electric field transition region which was calculated by Zhang and Fogler [25], taking into account the non-linear screening effect. With this identity, the width D is indeed expressed in terms of the junction parameters and the charge densities
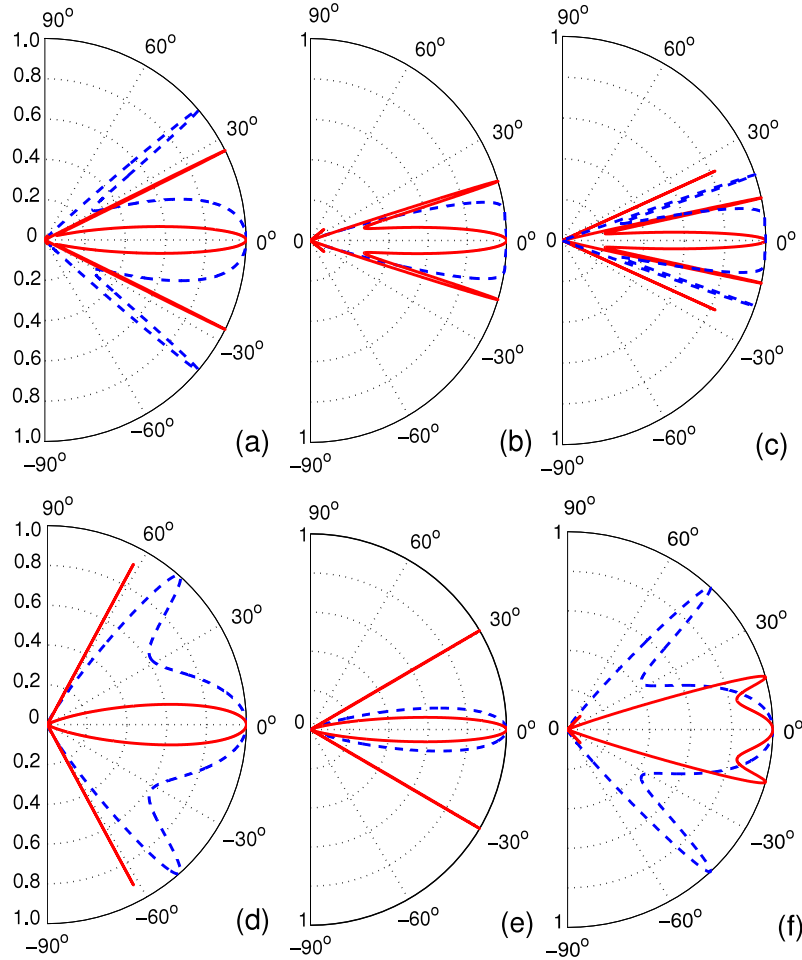
Figure 2. Polar graphs depicting $\mathcal{T}(\theta)$ for GBJs in rectangular potential model (dashed blue curves) and Gaussian-type potential model (solid red curves): the outmost semicircle corresponds to $\mathcal{T} = 1$ and the center to $\mathcal{T} = 0$ with grid spacing of 0.2; angles between $-\pi/2$ and $\pi/2$ are shown and the angular spacing is $\pi/6$. To see the role of each parameter, $\mathcal{T}(\theta)$-graphs are shown for various values of parameters [L (nm), E (meV), V_b (V), V_t (V)]: (a) [25, 0, 60, -12]; (b) [25, 50, 60, -12]; (c) [50, 50, 60, -12]; (d) [25, 0, 40, -6]; (e) [25, 50, 40, -6]; (f) [50, 0, 40, -6]. Note: due to the limiting scale of the figures some thin resonant peaks in the solid curves might be partly invisible; in reality, all the peaks reach the outmost semicircle (with $\mathcal{T} = 1$).

n_1 and n_2. Unfortunately, the expression $D(n_1, n_2)$ obtained in [25] becomes invalid at small values of n_1 or n_2, that leads to a divergence of resistances at the gate voltages, where a change in the junction charge density regime occurs (see figure 5(a) in [23]).

Recently, using the tight-binding model based quantum transport simulation [26], Liu and Richter calculated the GBJ conductance G as a function of the top gate voltage V_t and claimed a qualitative agreement between the calculated $G(V_t)$-dependences and the experimental data reported in [18].

For a smooth uni-junction (i.e. n–p junction) with $k_F D > 1$, the transmission probability was shown by Cheianov and Fal'ko [27] to be $\mathcal{T} = \exp[-\pi k_F D \sin^2 \theta]$. This $\mathcal{T}$-expression may be directly used to evaluate the resistance of GBJs if the top gate length L is larger than the carrier elastic mean free path l: $L > l$. In this case, after crossing the first transition region carriers lose all momentum information before entering the second one, and therefore, the total resistance of a GBJ can be modeled by the two isolated uni-junction (namely n–p and p–n) resistances in series. However, for the ballistic

GBJs of interest, when $L < l$, the device resistance should be consistently calculated for the whole structure, taking into account all possible reflections at transition regions as well as their interferences.

The aim of this paper is to re-examine the ballistic transport through locally gated GBJs, using an alternative model of a Gaussian-type potential barrier. This potential model has certain advantages: (i) it better reflects the potential profile in the real GBJs [4, 15], compared to the rectangular or the trapezoidal potential barrier model; (ii) for a given GBJ, the modeled potential barrier profile is entirely determined by the two gate voltages V_b and V_t, that provides a direct comparison of calculating transport properties to experimental data; and (iii) a continuous variation of the Gaussian-type potential as a function of space variables allows us to calculate the transport properties of heterojunctions in all possible charge density regimes, including a smooth transition between the regimes. In particular, using this potential model it is rather simple to calculate all transport characteristics of the GBJs under study.
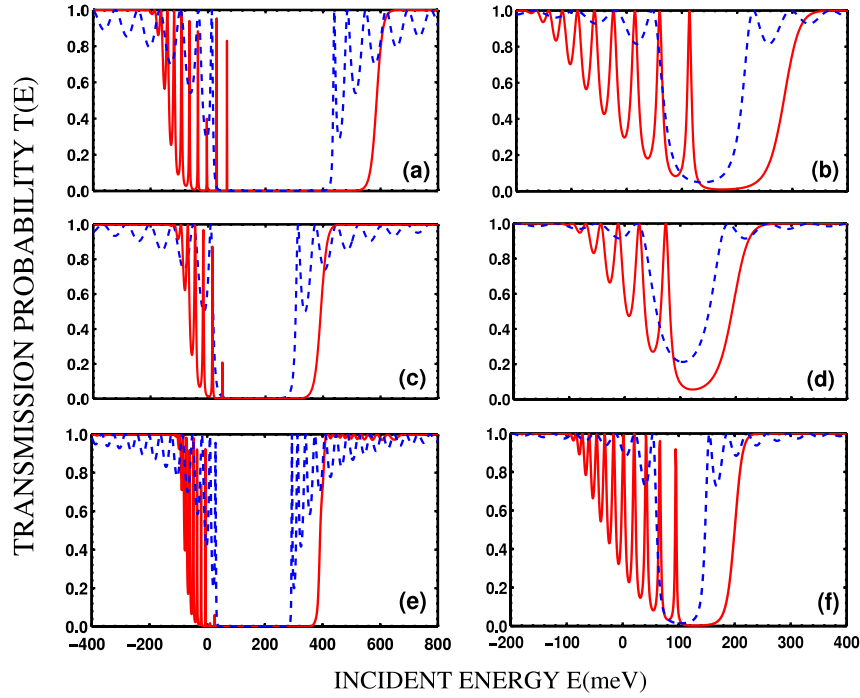
Figure 3. Transmission probabilities $\mathcal{T}$ for the same GBJs as discussed in figure 2 but plotted as a function of the incident energy E at various incident angles θ: dashed blue curves—$\mathcal{T}(E)$ in rectangular potential model; solid red curves—Gaussian-type potential model. (a)–(f) Various values of the parameters [L (nm), θ, V_b (V), V_t (V)]: (a) [25, $\pi/6$, 60, -12]; (b) [25, $\pi/18$, 60, -12]; (c) [25, $\pi/6$, 40, -6]; (d) [25, $\pi/18$, 40, -6]; (e) [50, $\pi/6$, 40, -6]; (f) [50, $\pi/18$, 40, -6]. Note: for the same reason of limiting figure scale as in figure 2, some thin resonant peaks in this figure might be partly invisible; in reality, all peaks should go to one.
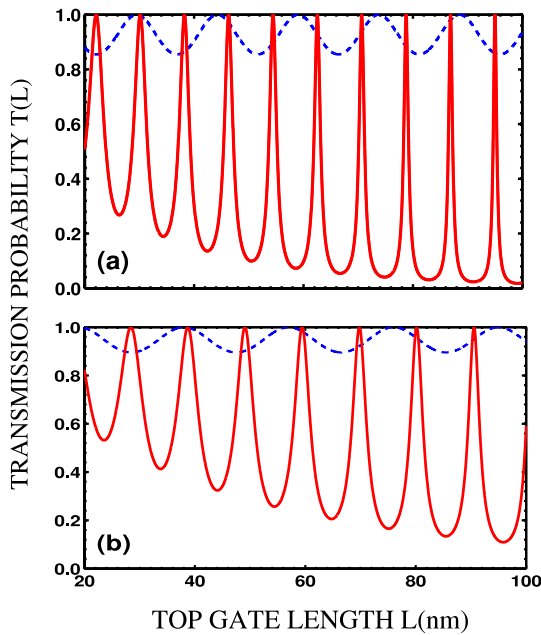

Figure 4. Transmission probability is plotted versus the length L for two GBJs of [V_b, V_t] = [60, -12] V (a) and [40, -6] V (b). In both blocks $E = 0$ and $\theta = \pi/18$; dashed blue lines—$\mathcal{T}(L)$ in rectangular potential model; solid red lines—Gaussian-type potential model.

Based on the potential model suggested, we systematically examined the zero-temperature ballistic transport properties of GBJs, using the T-matrix approach [29, 30] first to calculate the transmission probability, and then the Landauer formalism [31] to calculate the device resistance, the current and the shot noise. Obtained transmission probabilities are discussed in comparison with those of equation (1) for the rectangular barrier model to demonstrate the role of the Klein tunneling and the interference effects. Calculated resistances R describe well the typical experimental observations such as a reproducible oscillation of R against V_t or an asymmetry in the $R(V_t)$-curves with respect to the maxima. An associated oscillation observed in the zero-bias shot noise with respect to V_t is also in good agreement with experiments. The bias voltage modifies the potential barrier, leading to the current–voltage characteristics with a slightly negative differential resistance region and to the shot noise which is considerably suppressed in the low bias region and becomes fluctuating at higher biases.

This paper is organized as follows. Section 2 describes the model and calculation methods. Section 3 is devoted to present obtained results for the transmission probability. Section 4 is focused on the junction resistance. In section 5, the current–voltage (I–V) characteristics and the shot noise are addressed. Section 6 is a summary including an additional brief discussion.

2. Model and calculating method

By solving the two-dimensional Laplace equation with the potentials of the two gates as boundary conditions, Gorbachev *et al* have calculated the gates' induced potential profile along p–n–p junctions (x direction in figure 1). Calculations carried out at different gate voltages V_b and V_t show clearly an

inverse Gaussian-type shape of potential profile (see figures 3(b)–(d) in [15]). The Gaussian-type potential profile was further reported by Rossi *et al* in [28], where the ground state carrier density and the corresponding potential along the device have been calculated using the Thomas–Fermi–Dirac approximation. Liu and Richter also reported a similar potential profile in their quantum transport simulations [26]. These studies brought about the present idea of suggesting the Gaussian-type potential barrier model to describe transport properties in GBJs.

Structures under study are schematically drawn in figure 1(a), where L is the top gate length and the x-axis is directed along the graphene stripe with the origin ($x = 0$) located at the middle of the top gate (see figure 1(c)). Along the (unshown) transverse y-direction the width W of the stripe (and the gates) is assumed to be large compared to the top gate length. The voltages V_b and V_t applied respectively to the back gate and the top gate induce in the stripe a total potential which is here suggested to (i) be constant along the y-direction and (ii) vary along the x-direction as

$$U(x) = U_{21} \cdot e^{-x^2/\alpha L^2} + U_1, \qquad (3)$$

where $U_{21} = U_2 - U_1$ with $U_{1(2)}$ defined in the paragraph following equation (1) and α is a constant of the order of unity, which is perhaps dependent on the top gate length L. Note that the potentials $U_{1(2)}$ are entirely determined by the charge densities $n_{1(2)}$, which are in turn entirely determined by the gate voltages $V_{b(t)}$, given structural parameters of the junction (i.e. the width W, the length L, the capacitances $C_{t(b)}$ and the voltages $V_{t(b)}^{(0)}$).

Obviously, depending on the sign of the potential factor U_{21}, the suggested potential barrier of equation (3) has either a Gaussian-type or an inverse Gaussian-type shape with the maximum or the minimum at $x = 0$, where the potential is just equal to U_2. This means the quantity n_2 defined in equation (2) is just the charge density at $x = 0$. Beyond this point in both directions, the charge density varies with x in a way consistent with the potential profile. In far regions, $|x| \gg L$, the potential of equation (3) reduces to U_1, implying that the charge density in the bulk graphene stripe is just n_1 defined in equation (2). Thus, in contrast to the rectangular or the trapezoidal potential barriers, the present Gaussian-type potential model describes a continuous variation of the charge density between the bulk value n_1 at a distance and the value n_2 in the center of the device. In addition, for a given junction these densities n_1 and n_2 are entirely determined by the gate voltages, as can be seen in the relations of equation (2).

Concerning the constant α in the potential of equation (3), a simple electrostatic estimation can show a dependence of α on the top gate length L. So, presumably, α is an adjustable parameter. In calculations discussed below, for simplicity, α is taken to be 1 (the length L is assumed to be much larger than the inter-carbon distance in the graphene lattice).

As a demonstration, figure 1(d) presents several potential profiles $U(x)$ of equation (3) for the GBJs with the same $L = 20$ nm and the same $V_b = 40$ V, but under different top gate voltages V_t (given in the figure). Hereafter, for definition, we borrow from [13] the following values of device parameters:

$C_b = 14$ nF cm^{-2}, $C_t = 1.0 \times 10^2$ nF cm^{-2}, $V_b^{(0)} = 31.5$ V, and $V_t^{(0)} = -1.4$ V. This figure demonstrates how the junction charge density regime could be changed as only the top gate voltage V_t varies. It resembles well figures 3(b)–(d) in [15], figure 1(b) in [28], or figure 1(c) in [26].

By varying both the gate voltages, V_b and V_t, independently, the relations of equation (2) draw a full diagram of junction charge density regimes as can be seen in figure 1(b). Again, this figure resembles figure 3(b) in [13] or figure 1(d) in [15].

Actually, within the present model, to study transport characteristics for a given GBJ we have first to solve the Dirac equation for the Hamiltonian with the potential defined in equation (3). Here, for simplicity, we assume that (i) potential magnitudes $|U_{1(2)}|$ should be much smaller than the bandwidth of the bare graphene π-band, so all that we deal with is just associated with the first π-band; (ii) typical length scales of the potential of equation (3), including the top gate length, should be much larger than the inter-carbon distance in the graphene lattice, so the intervalley scatterings between the Dirac points at K and K′ can be omitted; and (iii) the width W of the graphene stripe should be much larger than the top gate length L, so all the edge-related effects can be neglected. Under these assumptions the low energy properties of charge carriers in the structure of interest can be well described by the massless Dirac-like Hamiltonian:

$$H = -\hbar v_F \vec{\sigma} \vec{\nabla} + U(x)I, \qquad (4)$$

where $\vec{\sigma} = (\sigma_x, \sigma_y)$ are Pauli matrices, I is the identity matrix, and $U(x)$ is the potential defined in equation (3).

The Hamiltonian of equations (4) and (3) could not be solved analytically. However, as discussed in detail in [32], the T-matrix approach, well known in semiconductor physics [29], seems to be of high effectiveness for solving such a Hamiltonian with a smooth one-dimensional potential $U(x)$. Indeed, in principle, any smooth one-dimensional potential can be approximately treated as a series of many step potentials so that within each step the potential can be considered constant. The overall T-matrix to be found is then simply given by multiplying the partial T-matrices for all these step potentials. On the other hand, for each step potential the partial T-matrix can be obtained from the solutions of the Hamiltonian of equation (4) on the left and the right sides (where the potential U is considered constant) by requiring an appropriate condition of continuity at the step interface. The calculation procedure is the same as that in semiconductor structures [29], but the continuity is here required only for the wavefunctions (by matching up the corresponding amplitudes). Fortunately, such a procedure of constructing the overall T-matrix for the potential $U(x)$ of interest can be easily realized on a computer without the need of explicitly writing down solutions of the Hamiltonian (4) for each step. Certainly, as a rule, to ensure the accuracy of the result obtained the convergence of the numerical solution should be carefully checked in each calculation.

Using the obtained overall T-matrix, the transmission probability $\mathcal{T}$ through the studied junction can be calculated

as a function of the incident energy E and the incident angle θ [32]:

$$\mathcal{T}(E,\theta) = \begin{cases} 1 - |T_{21}|^2/|T_{22}|^2, & \text{if } \lambda_L \lambda_R > 0 \\ 1 - |T_{22}|^2/|T_{21}|^2, & \text{otherwise,} \end{cases} \quad (5)$$

where T_{ij}, $(i,j=1,2)$ are elements of the T-matrix, $T = (T_{11}T_{12}; T_{21}T_{22})$, $\lambda_{L(R)} = \text{sign}(E - U_{L(R)})$ with $U_{L(R)}$ the potential in the left (right) lead.

Once the transmission probability $\mathcal{T}$ of equation (5) is known, one can within the framework of the Landauer formalism calculate the conductance [32]

$$G = \frac{ge^2 W}{v_F h^2} |\mu_0 - U_1| \int_{-\pi/2}^{\pi/2} d\theta \, \mathcal{T}(\theta) \cos\theta \quad (6)$$

and the zero-bias Fano factor [31]

$$\mathcal{F} = \frac{\sum_n \mathcal{T}_n (1 - \mathcal{T}_n)}{\sum_n \mathcal{T}_n}. \quad (7)$$

Here, the Fano factor $\mathcal{F}$ is as usual defined as the ratio of the actual shot noise power S and the Poissonian noise S_P that would be measured if the system produced noise due to single independent carriers. The sums in equation (7) are taken over all conduction channels. This expression of the zero-bias Fano factor $\mathcal{F}$ is most valid in the linear regime.

Beyond the linear regime, the bias voltage V_{sd} produces a considerable x-dependent addition to the potential of equation (3) and therefore modifies the profile of this potential. Nevertheless, with the same T-matrix approach as described above, the transmission probability can be equally calculated for such modified potential barriers, taking into account the bias voltage effects. Thus, for a given bias V_{sd}, we first calculate $\mathcal{T}(E,\theta)$, then within the framework of the Landauer formalism calculate the drain current [32]

$$I = \frac{geW}{v_F h^2} \int_{\mu_R}^{\mu_L} dE |E - U_1| \int_{-\pi/2}^{\pi/2} d\theta \, \mathcal{T}(E,\theta) \cos\theta, \quad (8)$$

and the bias-dependent shot noise power

$$S = 2\frac{geW}{v_F h^2} \int_{\mu_R}^{\mu_L} dE |E - U_1| \int_{-\pi/2}^{\pi/2} d\theta \, \mathcal{T}(E,\theta)$$
$$\times [1 - \mathcal{T}(E,\theta)] \cos\theta. \quad (9)$$

This noise power then determines the bias-dependent Fano factor $\mathcal{F} = S/S_P = S/2e\bar{I}$, where $\bar{I}$ the average current [31]. Thus, in this way, the current–voltage $I(V_{sd})$- and the Fano factor–voltage $\mathcal{F}(V_{sd})$-characteristics can be produced.

It should be here noted that in equations (6)–(9) $g = 4$ is the degree of degeneracy, W is the stripe width, and $\mu_{L(R)}$ is the Fermi energy at the left (right) lead. At equilibrium, the potentials in the left and right regions are of equal height and $\mu_L = \mu_R \equiv \mu_0$ (see equation (6)). A bias voltage V_{sd} causes a difference between μ_L and μ_R, $|\mu_L - \mu_R| = eV_{sd}$, and therefore induces a current.

Thus, given GBJ, i.e. given stripe width W, top gate length L, and gate voltages $V_{b(t)}$, the calculation procedure is as follows: (i) determine the potential of equation (3); (ii) solve the Hamiltonian of equation (4) using the T-matrix

approach to calculate the transmission probability of equation (5); and (iii) calculate the conductance of equation (6) and the zero-bias Fano factor of equation (7), using the Landauer formulas. Further, to study the current–voltage and the Fano factor–voltage characteristics, at each bias V_{sd} we have first to modify the potential barrier taking into account the bias effect, then calculate the transmission probability $\mathcal{T}(E,\theta)$ in the same way as in the case of zero bias, and then calculate the current of equation (8) and the shot noise power of equation (9). Calculations are carried out for the n–p–n junctions in the ballistic regime. In calculations, the values of $C_{b(t)}$ and $V_{b(t)}^{(0)}$ are as mentioned above borrowed from the experiment [13], the stripe width W is given to be large and fixed ($W = 3$ μm), and the gate length L is chosen between 20 and 100 nm, while the gate voltages $V_{b(t)}$ greatly vary.

3. Transmission: Klein tunneling and interference effects

Klein tunneling is a relativistic effect and has never been observed experimentally in particle, nuclear, or astro-physics. The fact that charge carriers in graphene are massless relativistic particles provides a possibility to test this effect in simple condensed-matter experiments. Following Katsnelson *et al* [7], a unique manifestation of Klein tunneling can be found in the incident-angle dependence of the transmission probability across a potential barrier created on a graphene sheet. We present such $\mathcal{T}(\theta)$-dependences in figure 2 for the GBJs modeled by either rectangular potentials (dashed blue lines) or Gaussian-type potentials of equation (3) (solid red lines). The graphs in this figures are arranged in the following way: three graphs in the same line ((a)–(c) or (d)–(f)) are associated with identical gate voltages V_b and V_t, but with different lengths L and/or incident energies E, while the two graphs in the same column are associated with the same L and E, but with different gate voltages. Thus, to see how some factor does affect the transmission probability we should compare the appropriate adjacent graphs.

Obviously, in any graph of figure 2 both solid and dashed lines show a complete transparency of barriers, $\mathcal{T} = 1$, for the normal incidence ($\theta \to 0$). This is a typical manifestation of Klein tunneling, regardless of the barrier shape as well as the barrier size. Nevertheless, as can be seen in each of these graphs, the highly transmitted angular region for the Gaussian-type potential (solid lines) is always considerably narrower than that for the corresponding rectangular one (dashed lines). The root cause of such a difference in the highly transmitted angular region between the two models is the smoothness of the Gaussian-type potential, which as well known strongly suppresses the Klein tunneling. On the other hand, since the smoothness of the potential of equation (3) mutually depends on the junction parameters (i.e. L, V_b, and V_t, see figure 1(d)), the relative Klein tunneling suppression of the two models should also depend on these parameters (compare the graphs in figure 2 to each other).

Another common feature observed in all the graphs in figure 2 is the symmetry of $\mathcal{T}$ with respect to the sign of θ, $\mathcal{T}(\theta) = \mathcal{T}(-\theta)$. Beyond the central region of perfect

transmission there are often resonances. Figure 2 also shows that these resonances are much narrower in the case of Gaussian-type potentials compared to the case of rectangular ones (see the note in the figure). Again, the root of this difference is the smoothness of the Gaussian-type potentials.

Since the only parameters distinguishing from each other the two graphs in the same column in figure 2 are the gate voltages ($(V_b, V_t) = (60, -12)$ V for all graphs in the first line and $(40, -6)$ V for the second line), comparing the two graphs in each column, (a)–(d), (b)–(e) or (c)–(f), shows how the incident-angular dependence of the transmission probability depends on the gate voltages. On the other hand, comparing the three graphs in each line to each other reveals the influence of the other two factors, the incident energy or the top gate length, on the θ-dependence of the tunneling process.

To see in detail the incident energy dependence of the transmission probability, we show in figure 3 the $\mathcal{T}(E)$-functions calculated for the same GBJs as those in figure 2 and in the two models, rectangular potential (dashed blue lines) and Gaussian-type potential (solid red lines). The panels in this figure are arranged in the following way: (i) the two panels in the same line are associated with the same junction (i.e. the same L, V_b, and V_t), but with different incident angles ($\theta = \pi/6$ for the three panels in the left column and $\theta = \pi/18$ for the right column), and (ii) in each column, the only difference between the top and the middle panel is the gate voltages, while that between the middle and the bottom panel is the top gate length.

The strong oscillation is the most impressive feature of all the $\mathcal{T}(E)$-curves shown in figure 3 for both rectangular and Gaussian-type potential models. Actually, this oscillation is the typical resonant picture originating from the interference effect that makes the potential barrier perfectly transparent at certain energies. Actually, figure 3 also shows an essential difference in the resonant picture between the two models considered. In reality, the distribution of resonant peaks in the transmission probability reflects the distribution of resonant levels inside the studied potential well/barrier. In the range of parameters examined in figure 3 the level distributions in rectangular potential barriers are more or less symmetric, and therefore the resonant pictures are almost symmetric, as can be seen in all panels in figure 3. In contrast, for the Gaussian-type potential barriers the resonant level distributions are strongly asymmetric. In the case of the n–p–n junctions studied here the resonant levels are much denser in the low energy region and therefore the resonant peaks in this region are highly dense, as shown by the solid lines in figure 3. Certainly, an inverse resonant picture should be observed in the case of p–n–p junctions, where the resonant peaks should be denser in the high energy region. Concerning the oscillation magnitude, due to a smoothness of the Gaussian-type potential in any graph in figure 3 the minima in the solid curve are always much deeper than those in the dashed one.

As already seen in figure 2, there is a close correlation between the two variables θ and E in affecting the transmission probability $\mathcal{T}$. Such a correlation becomes clearer in comparing the corresponding panels in the two

columns in figure 3. A decrease from $\theta = \pi/6$ (outside the highly transmitted angular regions in figure 2) in the left column to $\theta = \pi/18$ (inside the highly transmitted angular regions in figure 2) in the right column induces a remarkable change in the $\mathcal{T}(E)$-graphs (note the difference in energy scale for the graphs in the two columns.) In particular, there is always in the left column a large incident energy gap where $\mathcal{T} = 0$, whereas in the right column $\mathcal{T}$ is practically non-zero in the whole range of energy under study.

The only length scale in both models is the 'top gate length' L, which plays a key role in determining the resonant picture. Indeed, the only change of L from 25 to 50 nm results in a much higher frequency in the $\mathcal{T}$ versus E oscillations, as can be seen by comparing the middle panel with the bottom one in either column in figure 3, i.e. (c)–(e) or (d)–(f).

To learn more about the role of the length L in forming the tunneling process, we calculated $\mathcal{T}$ as a function of L and present in figure 4 the results obtained in two cases: (a) and (b), with the same gate voltages and incident angle as those in figures 3(b) and (d), respectively. Note that in contrast to figure 3 in [7], where the normally incident transport was examined, figure 4 is depicted in the case of $\theta = \pi/18$. In this case, equation (1) for rectangular potential barriers gives a sinusoidal dependence of $\mathcal{T}$ on L that is described by the dashed lines in figure 4. For the Gaussian-type potential barriers, as shown by the solid lines in figure 4, the $\mathcal{T}(L)$-curves are no longer exactly sinusoidal, though they still show an oscillation rather regular in L. In the ballistic regime, the only factor that could make $\mathcal{T}$ oscillate with respect to L is the reflection and interference processes. So, the $\mathcal{T}(L)$-oscillations observed in figure 4 could be seen as one more manifestation of the reflection and interference processes occurring inside potential barriers. Certainly, since the detailed shape of the potential barrier of equation (3) is also sensitive to the gate voltages, the reflection and interference processes should depend on these parameters too. This explains the observed difference between the two solid lines in figures 4(a) and (b). Besides, in consistency with the $\mathcal{T}$-oscillation shown in figure 3, in both figures 4(a) and (b) the solid line always oscillates more strongly and more frequently compared to the dashed one in the same figure.

The properties of the transmission probability stated above should be manifested in the fundamental transport characteristics such as the resistance $R = 1/G$, the current I and the Fano factor $\mathcal{F}$.

4. Resistances: theory versus experiments

A reproducible oscillation of the resistance R as a function of the top gate voltage V_t and an asymmetry of the $R(V_t)$-curve with respect to the maximum at the voltage V_t corresponding to $n_2 \approx 0$ are the two most typical properties of transport across GBJs reported in different experiments [12, 13, 15, 18].

Figure 5(a) presents calculated resistances $R = 1/G$ of equation (6) plotted against the top gate voltage V_t at different back gate voltages: $V_b = 40$ V (dash–dotted line), 60 V (solid line), and 80 V (dashed line). Experimentally, the back gate voltage V_b should be set first to produce the carrier type and
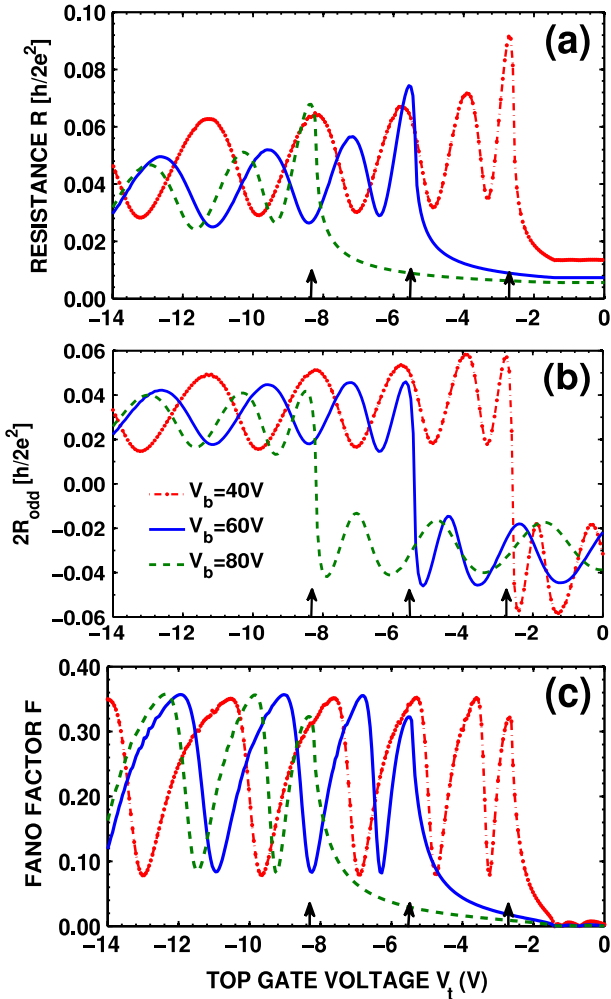
Figure 5. Resistances R (a), odd resistance $2R_{odd}$ (b), and zero-bias Fano factors $\mathcal{F}$ (c) versus V_t for three cases with $V_b = 40$ V (dash–dotted red lines), 60 V (solid blue lines), and 80 V (dashed green lines). Arrows indicate the transition top gate voltages $V_t^{(c)}$ where the transition between n–p–n and n–n$'$–n regimes occurs ($V_t^{(c)} = -2.59$ V, -5.39 V and -8.19 V for $V_b = 40$ V, 60 V and 80 V, respectively).

density n_1 in the graphene stripe. Then, the top gate can be set to create a bipolar junction and, further, can be varied to change the junction regime. For all the voltages V_b chosen in figure 5, the density n_1 is always positive, implying that the graphene stripes are always set in the n-regime. The voltage V_t is at the beginning set to a large negative value to produce a n–p–n junction with high potential U_2 (or large $|n_2|$, $n_2 < 0$). On increasing V_t in the positive direction, the density n_2 is gradually reduced in value, then vanishes at some transition top gate voltage $V_t = V_t^{(c)}$, where a change from the n–p–n to n–n$'$–n regime occurs. For the samples with $V_b = 40$ V, 60 V, and 80 V examined in figure 5, equation (2) gives $V_t^{(c)} = -2.59$ V, -5.39 V, and -8.19 V (indicated by arrows in the figure)

As is evident in figure 5(a), for a given V_b, the resistance R strongly oscillates with a slightly increasing average value as V_t increases in the region of $V_t < V_t^{(c)}$, when $n_1 n_2 < 0$, i.e. when the studied junction remains in the n–p–n regime.

Crossing the last maximum at $V_t \approx V_t^{(c)}$, the junction enters the n–n$'$–n regime, where the structure becomes much more transparent and consequently the resistance experiences a sharp reduction at $V_t > V_t^{(c)}$. In the range of V_b under study figure 5(a) also shows that an increase of V_b leads to a decrease of not only the transition voltage $V_t^{(c)}$, but also the average resistance in both regions, $V_t < V_t^{(c)}$ and $V_t > V_t^{(c)}$. On the whole, the calculated $R(V_t)$-dependences shown figure 5(a) describe quite well the experimental data reported in [12, 13, 15, 18].

Observed oscillations of R versus V_t can arise from the oscillations of the transmission probability caused by the inside-barrier interference of chiral waves [7]. It should be additionally noted that, within the Gaussian-type potential model, even if the gate length L is fixed ($L = 25$ nm for all curves in figure 5), the potential profile of equation (3) sensitively varies with the gate voltages. Such a potential profile variation induces a corresponding variation in the interference process, resulting in the observed differences in the oscillation manner (magnitude and 'period') between the curves in figure 5(a).

In each curve in figure 5(a), the last maximum located at $V_t \approx V_t^{(c)}$ separates the two junction regimes: the n–p–n on the left, where $n_1 \cdot n_2 < 0$, and the n–n$'$–n on the right, where $n_1 \cdot n_2 > 0$. The fact that for given absolute values of the densities n_1 and n_2 the resistance is always higher if $n_1 \cdot n_2 < 0$ than if $n_1 \cdot n_2 > 0$ makes any of the $R(V_t)$-curves in figure 5(a) asymmetric with respect to the last maximum. Such an asymmetry is seen as a typical character of GBJ resistances stated in a number of experiments [12, 13, 15].

In order to highlight the effect of the n–p/p–n interfaces, Huard *et al* specially extracted the odd part of the junction resistance, R_{odd}, which depends on the sign of the carrier density n_2:

$$2R_{odd}(n_1, n_2) = R(n_1, n_2) - R(n_1, -n_2). \qquad (10)$$

In figure 5(b) the calculated 'odd resistance' $2R_{odd}$ of equation (10) is shown as a function of V_t for the same samples as in figure 5(a). Note from equation (10) that $R_{odd}(n_1, n_2) = -R_{odd}(n_1, -n_2)$, so all the $2R_{odd}(V_t)$-curves should behave symmetrically with respect to the point $2R_{odd}(V_t = V_t^{(c)})$. Evidently, for each curve of a given V_b in figure 5(b), on the far left ($|V_t| \gg |V_t^{(c)}|$) the odd resistance becomes dominant and the quantity $2R_{odd}$ approaches the corresponding total resistance presented in figure 5(a). On the other side, $R_{odd} \to 0$ as $V_t \to V_t^{(c)}$ (indicated by arrows in the figure). Qualitatively, the $2R_{odd}(V_t)$-dependences as seen in figure 5(b) for samples of different V_b describe well the experimental data reported in [13].

5. Current and shot noise

In order to study the current–voltage (*I–V*) characteristics, it is assumed that a symmetric bias $[+eV_{sd}/2, -eV_{sd}/2]$ is applied to the two leads (source and drain), linked to the structure under measurement. For a given V_{sd}, the drain current I can be calculated using equation (7), where $\mathcal{T}(E, \theta)$
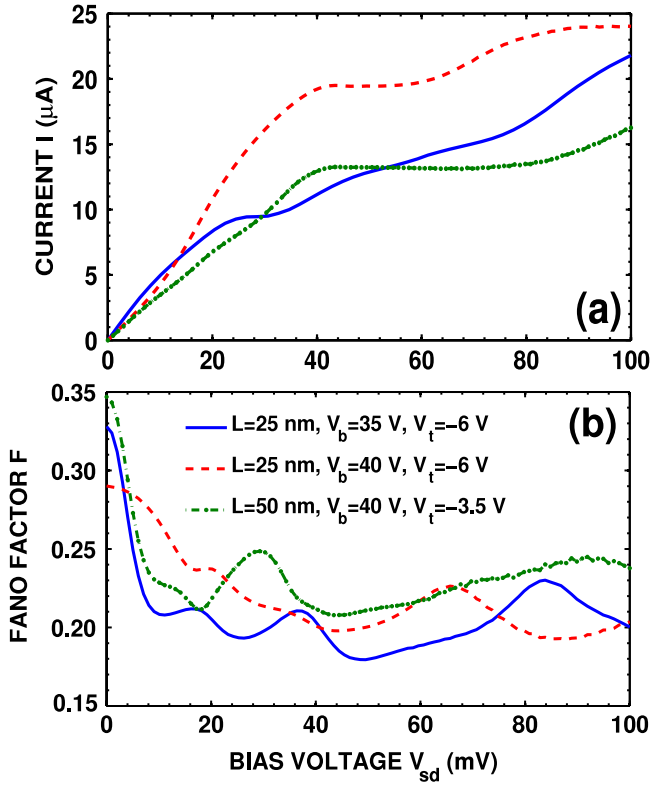
Figure 6. (a) Current–voltage and (b) Fano factor–voltage characteristics for three junctions with [L (nm), V_b (V), V_t (V)] = [25, 35, −6] (solid blue lines), [25, 40, −6] (dashed red lines) and [50, 40, −3.5] (dash–dotted green lines). The bias voltage V_{sd} is symmetrically applied to the source and the drain.

is the transmission probability of the potential barrier of equation (3), modified by the bias V_{sd}.

Figure 6(a) shows the *I–V* curves for three GBJs different in one or two parameter values as given in the figure. In general, by gradually rising the bias voltage V_{sd}, starting from $V_{sd} = 0$, the current I first increases progressively, then experiences a slowing down at some bias voltage, which mainly depends on the back gate voltage V_b, i.e. on the global carrier density n_1 in the stripe ($n_1 = 0.3 \times 10^{12}$ cm^{-2} for the solid line and 0.74×10^{12} cm^{-2} for the dashed and dash–dotted lines). Crossing this bias voltage, currents weakly fluctuate and even go through a slightly negative differential resistance (NDR) region. The position and the width of this NDR region depend on the junction parameters as can be seen in figure 6(a). Calculations reveal a close association between the observed NDR and the bias-dependence of the transmission probability. In any case, examining the *I–V* curves for a number of GBJs with different values of parameters, including V_b, V_t, L, and W also, shows that within the model of interest the NDR effect is always rather weak.

Finally, we study the shot noise. As a consequence of the quantization of charge, the shot noise yields transmission information that is not available from the conductance: the zero-frequency noise can probe the effects of disorder, carrier statistics, and interaction in nano-samples [31]. For the wide stripes of ballistic graphene ($W/L \geq 4$, where W is the width

and L the length of the stripe) the Fano factor $\mathcal{F}$ in the linear regime is predicted to be 1/3 at the charge-neutrality point and ∼0.12 in both n and p regimes [21]. This value of $\mathcal{F}$ is then suggested to be held in graphene double barrier structures [34]. Further, the value of $\mathcal{F} = 1 - 1/\sqrt{2} \approx 0.29$ is predicted for the shot noise across a ballistic n–p junction [27]. Moreover, the value $\mathcal{F} \approx 0.30$ is also predicted for strong, smooth 'charge-puddle' disorders, both at and away from the charge-neutrality point [35]. Experimentally, while the shot noise of $\mathcal{F} = 1/3$ has been observed in wide ballistic two-terminal graphene devices [33], the theoretical value $\mathcal{F} \approx 0.29$ is considerably lower than the experimental value of ∼0.38 reported for both p–n and n–p samples [36].

Within our potential model the zero-bias Fano factor of equation (7) is depicted in figure 5(c) as a function of the top gate voltage V_t for the same GBJs with resistances analyzed in figures 5(a) and (b). All the $\mathcal{F}(V_t)$-curves in figure 5(c) show the common features as follows: (i) in the n–p–n regime of $V_t < V_t^{(c)}$ (indicated by the corresponding arrow), the Fano factor $\mathcal{F}$ strongly oscillates against V_t in accordance with the oscillation of the corresponding resistance in figure 5(a), (ii) in this rather regular oscillation $\mathcal{F}$ varies between the equal maxima of ≈0.36 and the equal minima of ≈0.08, and (iii) in the n–n′–n regime of $V_t > V_t^{(c)}$, the noise fast moves down to the zero noise, $\mathcal{F} = 0$, which should be realized in the limiting case when all channels are perfectly transparent. While the observed harmony of oscillations in resistance R (figure 5(a)) and in Fano factor $\mathcal{F}$ (figure 5(c)) of the same GBJ is quite well understood [31], the fact that all three curves for various GBJs in figure 5(c) exhibit practically the same maxima of 0.36 and the same minima of 0.08 causes a little surprise. In any case, this value of $\mathcal{F} = 0.36$ is rather close to the experimental value of 0.38 claimed in [36]. Actually, on the whole, the $\mathcal{F}(V_t)$-curves shown in figure 5(c) are quite similar to that obtained for the trapezoidal potential barrier model in [22].

Thus, our model provides the shot noise with $\mathcal{F} \approx 0.36$ for n–p–n GBJs in the linear regime. A question might then arise of whether the bias voltage which modifies the potential barrier and changes the transmission probability can enhance the noise or even cause a super-Poissonian noise as it did in conventional semiconductor/metal nanostructures [37]. To shed light on this question, we show in figure 6(b) the $\mathcal{F}(V_{sd})$-characteristics for the same GBJs with *I–V*-characteristics presented in figure 6(a). So, it is useful to make a comparison between the two curves, $I(V_{sd})$ and $\mathcal{F}(V_{sd})$, for the same junction to gain possible correlations between the two characteristics. Actually, figure 6(b) demonstrates that for a given junction, in accordance with the current fluctuation in figure 6(a), the Fano factor, starting from the value $\mathcal{F}(V_{sd} = 0)$, fluctuates against the bias between the values ∼0.18 and ∼0.25. Noticeably, though the starting values of $\mathcal{F}$ at zero bias are different, with increasing bias voltage V_{sd} all three curves in figure 6(b) soon become fluctuating within almost the same range of magnitudes. Besides, comparing the $I(V_{sd})$-curve in figure 6(a) and the $\mathcal{F}(V_{sd})$-curve in figure 6(b) for the same sample also shows that the noise fluctuation is always much more profound, compared to the current one.

6. Conclusion

We have suggested an alternative model of Gaussian-type potential to describe transport properties of the locally gated GBJs. The advantage of this model consists in its reality and simplicity as well as its ability to describe GBJs in all possible charge density regimes, including smooth transitions between these regimes. Using the suggested model we have systematically studied the transmission probability $\mathcal{T}$, the resistance R, the current–voltage characteristics, and the shot noise for ballistic GBJs of different top gate lengths under largely varying gate voltages at zero temperature. An analysis of $\mathcal{T}$ calculated as a function of various parameters such as the incident angle, the incident energy, or the top gate length reveals multifarious manifestations of the Klein tunneling and the inside-barrier interference effects. Certainly, these effects should also be manifested in the junction resistance R, which shows a strong oscillation with respect to V_t in the n–p–n charge density regime and an asymmetry with respect to the maximum located at the top gate voltage where the n–p–n to n–n′–n regime transition occurs. Observed properties of calculated R as well as those of the odd part of resistances, R_{odd}, are all in good agreement with experiments. In accordance with the resistances, the zero-bias Fano factor experiences an equal oscillation between the maxima of 0.36 and the minima of 0.08 in the n–p–n regime and vanishes in the n–n′–n regime, regardless of junction parameters. With increasing bias voltage V_{sd}, the Fano factor, starting from the value $\mathcal{F}(V_{sd} = 0)$, becomes fluctuating with respect to bias. This noise fluctuation does correlate with the current fluctuation in the current–voltage characteristics, which often shows a slightly negative differential resistance region.

Numerical results shown in this work are focused on the junctions in the n–p–n regime. In fact, the Gaussian-type potential model deals equally with junctions in all possible regimes, including continuous transitions between them. Hopefully, this model might also be useful for describing transport properties in different types of locally gated bipolar junction, such as bilayer graphene or graphene based ones.

Acknowledgments

References

[1] Novoselov K S, Geim A K, Morosov S V, Jiang D, Zhang Y, Dubonos S V, Grigorieva I V and Firsov A A 2004 *Science* **306** 666
[2] Castro Neto A H, Guinea F, Peres N M R, Novoselov K S and Geim A K 2009 *Rev. Mod. Phys.* **81** 109
[3] Peres N M R 2010 *Rev. Mod. Phys.* **82** 2673
Peres N M R 2009 *J. Phys.: Condens. Matter* **21** 323201
[4] Das Sarma S, Adam S, Hwang E H and Rossi E 2011 *Rev. Mod. Phys.* **83** 407
[5] Avouris P, Chen Z H and Perebeinos V 2007 *Nature Nanotechnol.* **2** 605
[6] Ando T and Nakanishi T 1998 *J. Phys. Soc. Japan* **67** 1704
[7] Katsnelson M I, Novoselov K S and Geim A K 2006 *Nature Phys.* **2** 620
[8] Zhang Z, Tan Y W and Kim P 2005 *Nature* **438** 201
[9] Novoselov K S, Geim A K, Morosov S V, Jiang D, Katsnelson M I, Grigorieva I V, Dubonos S V and Firsov A A 2005 *Nature* **438** 197
[10] Cheianov V V, Fal'ko V and Altshuler B L 2007 *Science* **315** 1252
[11] Ozyilmaz B, Jarllo-Herrero P, Efetov D, Abanin D A, Leviov L S and Kim P 2007 *Phys. Rev. Lett.* **99** 166804
[12] Stander N, Huard B and Goldhaber-Gordon D 2009 *Phys. Rev. Lett.* **102** 026807
[13] Huard B, Sulpizio J A, Stander N, Todd K, Yang B and Goldhaber-Gordon D 2007 *Phys. Rev. Lett.* **98** 236803
[14] Williams J R, DiCarlo L and Marcus C M 2007 *Science* **317** 638
[15] Gorbachev R V, Mayorov A S, Savchenko A K, Horsell D W and Guinea F 2008 *Nano Lett.* **8** 1995
[16] Liu G, Velasco J, Bao W Jr and Lau C N 2008 *Appl. Phys. Lett.* **92** 203103
[17] Liu X, Oostinga J B, Morpurgo A F and Vandersypen L M K 2009 *Phys. Rev. B* **80** 121407
[18] Young A F and Kim P 2009 *Nature Phys.* **5** 222
[19] Belotin E B, Sikes K J, Hone J, Stormer H L and Kim P 2008 *Phys. Rev. Lett.* **101** 096802
[20] Du X, Skachko I, Barker A and Andrei E Y 2008 *Nature Nanotechnol.* **3** 491
[21] Tworzydlo J, Trauzettel B, Titov M, Rycerz A and Beenakker C W J 2006 *Phys. Rev. Lett.* **96** 246802
[22] Sonin E B 2009 *Phys. Rev. B* **79** 195438
[23] Low T, Hong S, Appenzeller J, Datta S and Lundstrom M 2009 *IEEE Trans. Electron Devices* **56** 1292
[24] Sauter F 1931 *Z. Phys.* **69** 742
[25] Zhang L M and Fogler M M 2008 *Phys. Rev. Lett.* **100** 116804
[26] Liu M-H and Richter K 2012 *Phys. Rev. B* **86** 115455
[27] Cheianov V V and Fal'ko V I 2006 *Phys. Rev. B* **74** 041403(R)
[28] Rossi E, Bardarson J H, Brouwer P W and Das Sarma S 2010 *Phys. Rev B* **81** 121408(R)
[29] Davies J H 1998 *The Physics of Low-Dimensional Semiconductors. An Introduction* (Cambridge: Cambridge University Press)
[30] Nguyen H C, Hoang M T and Nguyen V L 2009 *Phys. Rev. B* **79** 035411
[31] Blanter Ya and Büttiker M 2000 *Phys. Rep.* **336** 1
[32] Nguyen H C and Nguyen V L 2009 *J. Phys.: Condens. Matter* **21** 045305
[33] Danneau R, Wu F, Craciun M F, Russo S, Tomi M Y, Salmilehto J, Morpurgo A F and Hakonen P J 2008 *Phys. Rev. Lett.* **100** 196802
[34] Zhu R and Guo Y 2007 *Appl. Phys. Lett.* **91** 252113
[35] San-Jose P, Prada E and Golubev D S 2007 *Phys. Rev. B* **76** 195445
[36] DiCarlo L, Williams J R, Zhang Y, McMlure D T and Marcus C M 2008 *Phys. Rev. Lett.* **100** 156801
[37] Nguyen V H and Nguyen V L 2006 *Phys. Rev. B* **73** 165327